ACS Catalysis

Research Article

pubs.acs.org/acscatalysis

Tuning Electronic Structures of Nonprecious Ternary Alloys Encapsulated in Graphene Layers for Optimizing Overall Water Splitting Activity

Yang Yang,[†] Zhiyu Lin,[†] Shiqi Gao,[†] Jianwei Su,[†] Zhengyan Lun,[†] Guoliang Xia,[†] Jitang Chen,[†] Ruirui Zhang,[†] and Qianwang Chen*[,†,‡]

[†]Hefei National Laboratory for Physical Science at Microscale, Department of Materials Science & Engineering, and Collaborative Innovation Center of Suzhou Nano Science and Technology, University of Science and Technology of China, Hefei 230026, China

[‡]High Magnetic Field Laboratory, Hefei Institutes of Physical Science, Chinese Academy of Sciences, Hefei 230031, China

Supporting Information

ABSTRACT: Electrochemical water splitting is considered as the most promising technology for hydrogen production. Considering overall water splitting for practical applications, catalysis of the oxygen evolution reaction (OER) and hydrogen evolution reaction (HER) should be performed in the same electrolyte, especially in alkaline solutions. However, designing and searching for highly active and inexpensive electrocatalysts for both OER and HER in basic media remain significant challenges. Herein, we report a facile and universal strategy for synthesizing nonprecious transition metals, binary alloys, and ternary alloys encapsulated in graphene layers by direct annealing of metal−organic frameworks. Density functional theory calculations prove that with an increase in the degree of freedom of alloys or a change in the metal proportions in FeCoNi ternary alloys, the electronic structures of materials can also be tuned intentionally by changing the number of transferred electrons between alloys and graphene. The optimal material alloys FeCo and FeCoNi exhibited remarkable catalytic performance for HER and OER in 1.0 M KOH, reaching a current density of 10 mA cm^{-2} at low overpotentials of 149 mV for HER and 288 mV for OER. In addition, as an overall alkaline water electrolysis, they were comparable to that of the Pt/RuO_2 couple, along with long cycling stability.

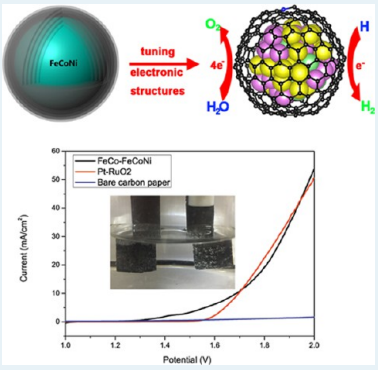

KEYWORDS: *water splitting, ternary alloy, graphene, tuning electronic structure*

Electrochemical water splitting is considered as the most promising technology for hydrogen production.[1−4] The overall water splitting consists of the oxygen evolution reaction (OER) on the anode and the hydrogen evolution reaction (HER) on the cathode, both of which need highly active catalysts to reduce the energy needed for water splitting via reducing their overpotential.[5] Precious metals and metal oxides such as Pt/C and Ir/C (or RuO_2) are state-of-the-art catalysts for HER and OER; however, their widespread practical application is hindered by their high cost and scarcity. Great effort has been spent over the past several decades in searching for nonprecious catalysts for HER or OER, but this area still lacks promising efficient catalysts that be commercialized on a large scale.[4,5] In addition, to realize continual overall water splitting for real applications, the catalysts for OER and HER should be operated under the same electrolyte, especially in an alkaline solution.[2] Nevertheless, challenges remain for most of the earth-abundant catalysts because of their incoordination with the PH ranges in which they exhibit excellent stability and activity.[1,3,6] Despite some progress in recent years, highly active and cost-effective catalysts that are efficient for both HER and OER in alkaline electrolytes with excellent activity and stability are still in great demand.[2,3]

Among many nonprecious materials, transition metals such as Fe, Co, and Ni and their alloys are regarded as potential substitutes for precious catalysts.[7−10] The combination of transition metals with graphene layers is beneficial for improving catalytic activity and stability.[11,12] Even though some studies have successfully synthesized various transition metals or alloys as efficient HER or OER catalysts, most of them are pure metals or binary alloys that can catalyze only one kind of electrochemical reaction in a certain solution, hindering their practical application in full water electrolysis.[9,11,13−15] Besides, the synergistic effects among Fe, Ni, and Co in the alloy are rarely reported in the literature. Previous studies have proved that incorporating transition metals into alloys will alter the lattice and bond length of the crystal to change the adsorption energies toward optimal catalytic activity.[12,16] Furthermore, it might provide a greater chance to alter the catalytic activity through changing the relative metal proportion in alloys due to the increased degree of freedom of alloys compared to those of pure metals.[17] Inspired by this, we can

Received: September 8, 2016
Revised: November 24, 2016
Published: December 2, 2016

DOI: 10.1021/acscatal.6b02573
ACS Catal. 2017, 7, 469−479

Scheme 1. Synthesis of Graphene Layer-Encapsulated FeCoNi Ternary Alloys[a]

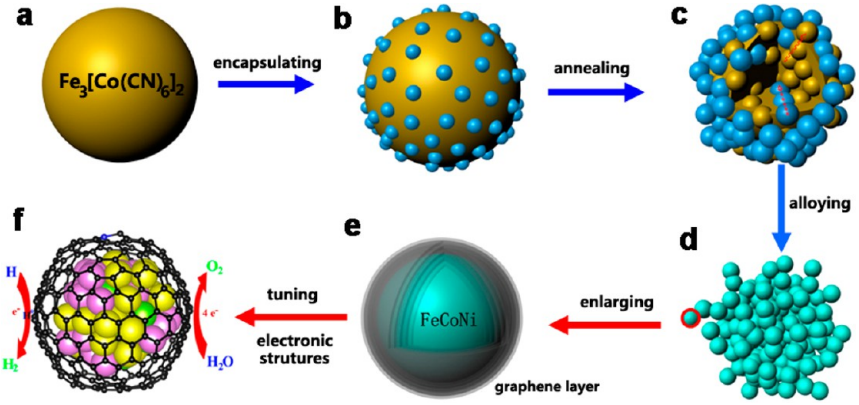

[a](a) $Fe_3[Co(CN)_6]_2$ sphere. (b) $Fe_3[Co(CN)_6]_2$ sphere encapsulated by $Ni_3[Co(CN)_6]_2$ small particles. (c) Metal interdiffusion during the annealing process, where dashed lines are possible diffusion paths of metal ions. (d) Finally, FeCoNi tenary alloy aggregates derived from the MOF precursor. (e) Enlarged model of an FeCoNi alloy particle encapsulated in nitrogen-doped graphene layers. (f) Tuning electronic structures of graphene-encapsulated alloys to optimize overall water splitting activity, where the yellow, pink, and green spheres represent Fe, Co, and Ni atoms, respectively.

anticipate that building more complex alloy compositions (from binary to ternary) would provide more possibilities of further enhancing the electrocatalytic performance via tuning metal compositions and proportions. However, hindered by the complex and tedious synthesizing process, few studies have focused on the graphene-encapsulated nonprecious ternary alloys, especially the elaborate tuning of electronic structure and a systematic study of the relationship between metal composition and overall water splitting activity.

To synthesize various catalysts with similar morphologies from a single precursor, our method is of great significance, especially with respect to building the relationship between composition and activity among different catalysts.[18] Metal–organic frameworks (MOFs) with a large surface area and tunable chemical structures have recently attracted a great deal of attention.[15,19−22] The tunable metal ion centers (such as Fe, Co, Ni, and Cu) and the design of organic ligands with different dopants (N, P, and S atoms) produce a perfect precursor for synthesizing encapsulated alloys with different metal compositions. Recently, our group has successfully synthesized FeCo alloys encapsulated in nitrogen-doped graphene layers by directly annealing the $Fe_3[Co(CN)_6]_2$ precursor, which shows excellent HER catalytic activity and stability.[12] MOF precursors can also be modified in many ways to obtain more complex compositions and structures.[23] Lou and his co-workers prepared Fe_3C@N-CNT from a dual MOF, which exhibits excellent electrochemical activity.[24] MOF-derived core–shell structures have also become very popular recently; however, confined by a single-metal or bimetal organic framework precursor, most of the derived materials are pure metal or at most binary alloys. Furthermore, few works have aimed to enhance electrochemical activity by increasing the degrees of freedom of alloys.

In this work, the available inherent MOF $Fe_3[Co(CN)_6]_2$ surface was used as an active support to load another MOF precursor, $Ni_3[Co(CN)_6]_2$. During the calcination process, the different metal ions will migrate to each other to form ternary alloys with an increasing annealing temperature; meanwhile, some CN^- groups in the MOF precursor will be catalyzed to form in situ nitrogen-doped graphene layers outside the alloy particles. Furthermore, the proportion of different metal ions can also be controlled by the relative proportion of the core and shell precursor. The materials of various alloys and metal proportions exhibit different HER and OER performances. We have obtained the relationship between activity and composition as well as the proportion of alloys through density function theory (DFT) calculations. It turns out the electronic structures of materials can also be tuned intentionally by changing the number of transferred electron between alloys and graphene. The optimal alloy catalysts for overall water splitting are also obtained via tuning electronic structures, which is even better than the Pt/RuO_2 counterpart.

To synthesize different nonprecious metals and alloys through same process, herein, we introduce a facile and universal method for the preparation of nitrogen-doped graphene-encapsulated uniform 3d transition metals, including pure metal, binary alloys, and ternary alloys, with various metal proportions by direct annealing of different MOFs. The samples obtained with different metal compositions were designated Co, FeCo, FeNi, CoNi, and FeCoNi, corresponding to different alloys encapsulated in nitrogen-doped graphene layers. Meanwhile, FeCoNi-1, FeCoNi-2, and FeCoNi-3 represent ternary alloys with different metal proportions. The detailed synthetic information and metal proportions can be seen in the Supporting Information. The ternary alloys with different metal proportions were fabricated as illustrated in Scheme 1. First, $Fe_3[Co(CN)_6]_2$ spheres were synthesized and used as core seeds to prepare the encapsulated MOF structure (Scheme 1a). Because of the similar crystal structure and lattice constant of Prussian blue analogues, it is possible to deposit relative small $Ni_3[Co(CN)_6]_2$ particles onto the large and clean spherical seeds to form a thin layer (Scheme 1b). In this process, polyvinylpyrrolidone (PVP) surfactant will control the morphology of particles while decreasing the speed of coordination between the metal ions and ligands, providing the opportunity for nucleation at the seed. During the thermal treatment, because of the nonequilibrium interdiffusion process of metal atoms and the porous structure of MOFs, the Fe, Co, and Ni metal ions would migrate to each other to form FeCoNi alloys during calcinations as illustrated in panels c and d of Scheme 1. At the same time, some CN^- group linkers will serve as both carbon and nitrogen sources for the in situ formation of

DOI: 10.1021/acscatal.6b02573
ACS Catal. 2017, 7, 469−479

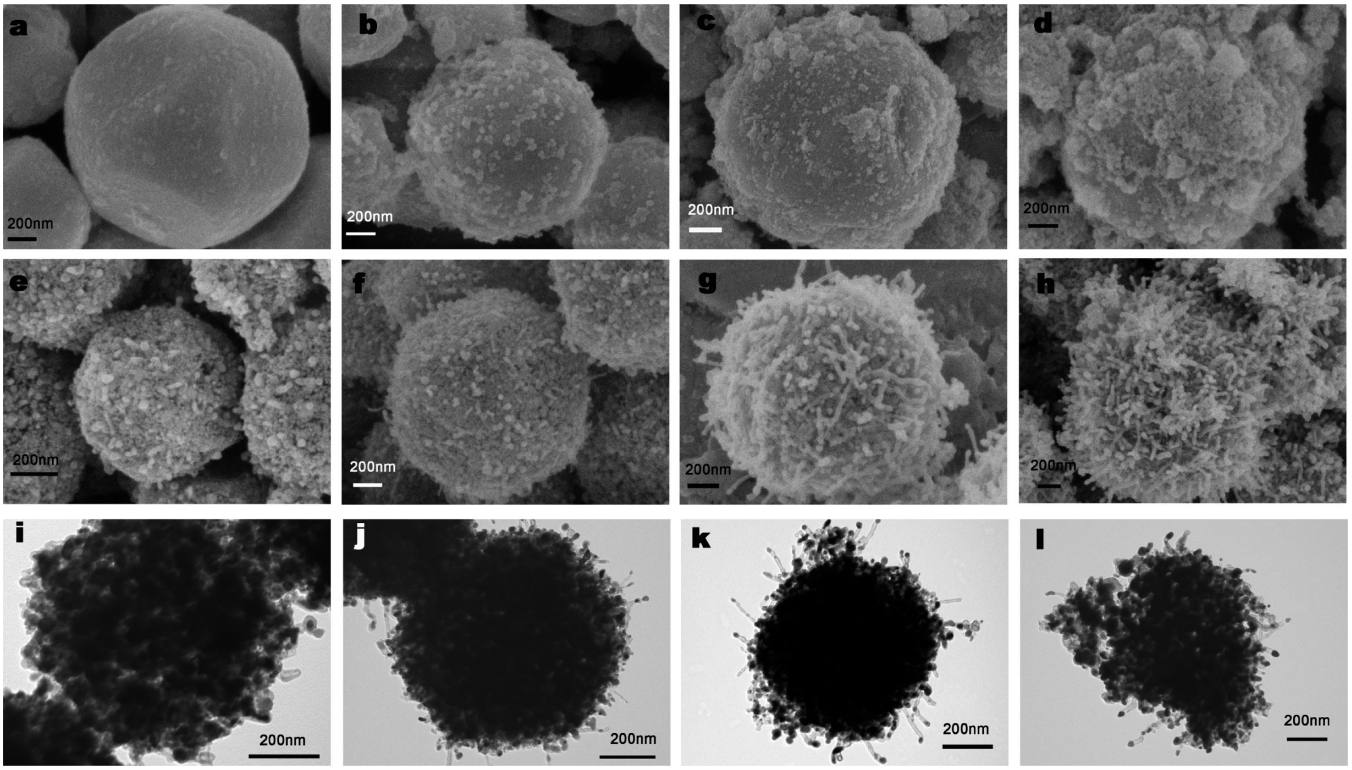

Figure 1. (a–d) Field emission scanning electron microscopy of pure $Fe_3[Co(CN)_6]_2$ and $Fe_3[Co(CN)_6]_2$ spheres encapsulated by increasing amounts of $Ni_3[Co(CN)_6]_2$. (e–h) SEM images of FeCo, FeCoNi-1, FeCoNi-2, and FeCoNi-3, respectively, by annealing of their corresponding precursors. (i–l) Transmission electron microscopy images of FeCo, FeCoNi-1, FeCoNi-2, and FeCoNi-3, respectively.

nitrogen-doped graphene layers outside the alloy particles. Scheme 1e is an enlargement of one FeCoNi particle encapsulated by nitrogen-doped graphene layers. Moreover, with a change in the amount of seeds and $Ni_3[Co(CN)_6]_2$ shell, the proportion of metals in ternary alloys can also be changed (Scheme 1f), thereby tuning the electronic structure of the material and optimizing its overall water splitting activity.

The sample of the $Fe_3[Co(CN)_6]_2$ seed showed a spherelike morphology with a diameter of approximately 600–1000 nm with a clean surface (Figure 1a) according to the field emission scanning electron microscopy (FESEM) results. With the addition of increasing amounts of $Ni_3[Co(CN)_6]_2$, the surfaces became more rough and the spherical seeds were encapsulated by more $Ni_3[Co(CN)_6]_2$ precursors as shown in Figure 1b–d. The annealing temperature of precursors was set to 600 °C, which proved to be the optimal annealing temperature for the Prussian blue analogue.[12] After being annealed, all the samples (Figure 1e–h) retained the morphology of their precursors. However, the samples with greater Ni content possessed more tubular margins at the edge of the sphere (Figure 1g,h). MOFs with a high Ni content are likely to form carbon nanotubes during the calcination process.[25] Panels i–l of Figure 1 are the transmission electron microscopy (TEM) images of FeCo, FeCoNi-1, FeCoNi-2, and FeCoNi-3, respectively, which reveal the spherical samples are composed of small encapsulated alloy particles. SEM and TEM images of Co, CoNi, and FeNi are provided in Figure S1.

High-resolution transmission electron microscopy (HRTEM) characterizations of ternary FeCoNi alloys (Figure 2 and Figures S2 and S3) indicate the alloys were completely encapsulated by graphene layers. As shown in panels a and b of Figure 2, the thickness of graphene layers is around 1.71 nm,

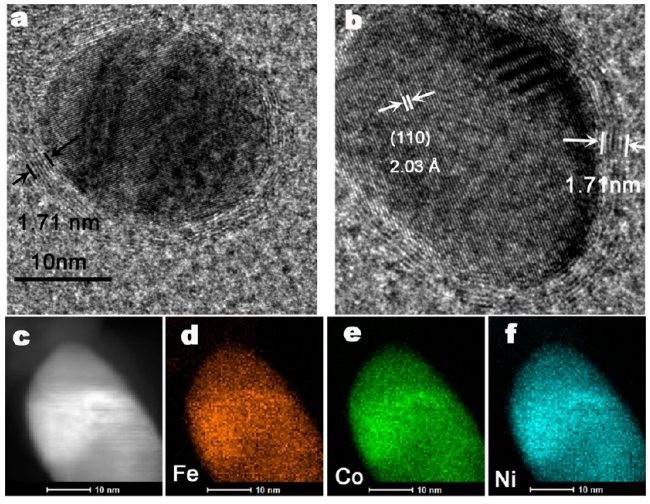

Figure 2. (a and b) Enlarged high-resolution transmission electron microscopy images of FeCoNi-1, where the interplanar spacing of the alloy as well as the graphene layers was measured. (c) STEM image of the single FeCoNi nanocrystal and the images of elemental mapping of (d) Fe, (e) Co, and (f) Ni.

corresponding to approximately five layers of graphene. Bao's group and our previous study proved an electron of the metal core could penetrate several layers of the graphene shell to promote the catalytic process while the graphene layer is also beneficial to catalytic stability.[12,16] Therefore, such an alloy core with a graphene shell structure is desirable for electrocatalysts. In addition, FeCoNi-1 exhibits a *d* spacing of 2.03 Å, in good agreement with the (110) plane of the FeCo alloy, indicating Ni atoms might be doped in the FeCo crystal lattice in

DOI: 10.1021/acscatal.6b02573
ACS Catal. 2017, 7, 469–479

FeCoNi-1. Panels c–f of Figure 2 are the images of elemental mapping by energy-filtered TEM (EFTEM), which reveals the Fe, Co, and Ni elements are uniformly distributed in the particles, further confirming the alloy structure of FeCoNi-1. The same results also appear in Figures S2 and S3, proving the successful fabrication of FeCoNi ternary alloys using a MOF precursor.

The crystal structures of metals, binary alloys, and ternary alloys were further confirmed by XRD results as illustrated in Figure 3. The graphite peaks in the XRD patterns are submerged because of the high intensity of alloy peaks. In fact, the enlarged patterns of ternary alloys in Figure 3 and the XRD pattern of FeCoNi-2 after acid treatment are illustrated in Figure S4, which shows a typical peak of C (002), indicating alloys are wrapped with graphene layers. The FeNi sample shows characteristic peaks at 51.8 and 76.4, corresponding to (200) and (220) planes of the FeNi alloy, respectively. The characteristic peaks for sample FeCo are at 44.8 and 65.3, which are assigned to the (110) and (200) planes of the FeCo alloy, respectively. The peaks of CoNi are similar to that of Co, indicating the Ni atoms might replace some of the Co atoms in the crystal of CoNi. The atomic radius of Co (1.67 Å) is larger than that of Ni (1.62 Å), and after incorporation of Ni atoms, the peaks of CoNi move slightly to higher degrees compared with those of Co. The XRD patterns of ternary alloys display characteristic reflections of the face-centered cubic (black color) phase and the body-centered cubic (blue color) phase of the $Fe_xCo_yNi_{100-x-y}$ alloy (especially for FeCoNi-2 and FeCoNi-3), which is consistent with previous studies.[26,27] In addition, the peak intensity ratio of body-centered cubic (1 1 0) to face-centered cubic (1 1 1) decreased from FeCoNi-1 to FeCoNi-3. The phenomenon indicates that the Fe content is decreased while the Ni content is increased from FeCoNi-1 to FeCoNi-3. This tendency is also consistent with the corresponding amount of metal of their MOF precursors.

The Raman spectra of ternary alloys and binary alloys are provided in Figure S5. All the samples displayed three Raman peaks located around 1349, 1583, and 2700 cm^{-1}, which correspond to the D, G, and 2D bands of carbon, respectively. The high I_D/I_G band intensity ratio of samples indicated the generation of large amounts of defects, suggesting a large

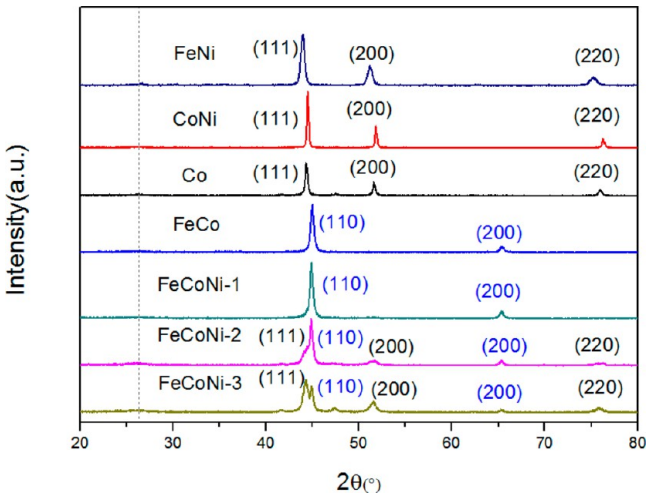

Figure 3. XRD patterns of various metals, binary alloys, and ternary alloys derived from MOF precursors. Black and blue colors refer to the face-centered cubic phase and body-centered cubic phase, respectively.

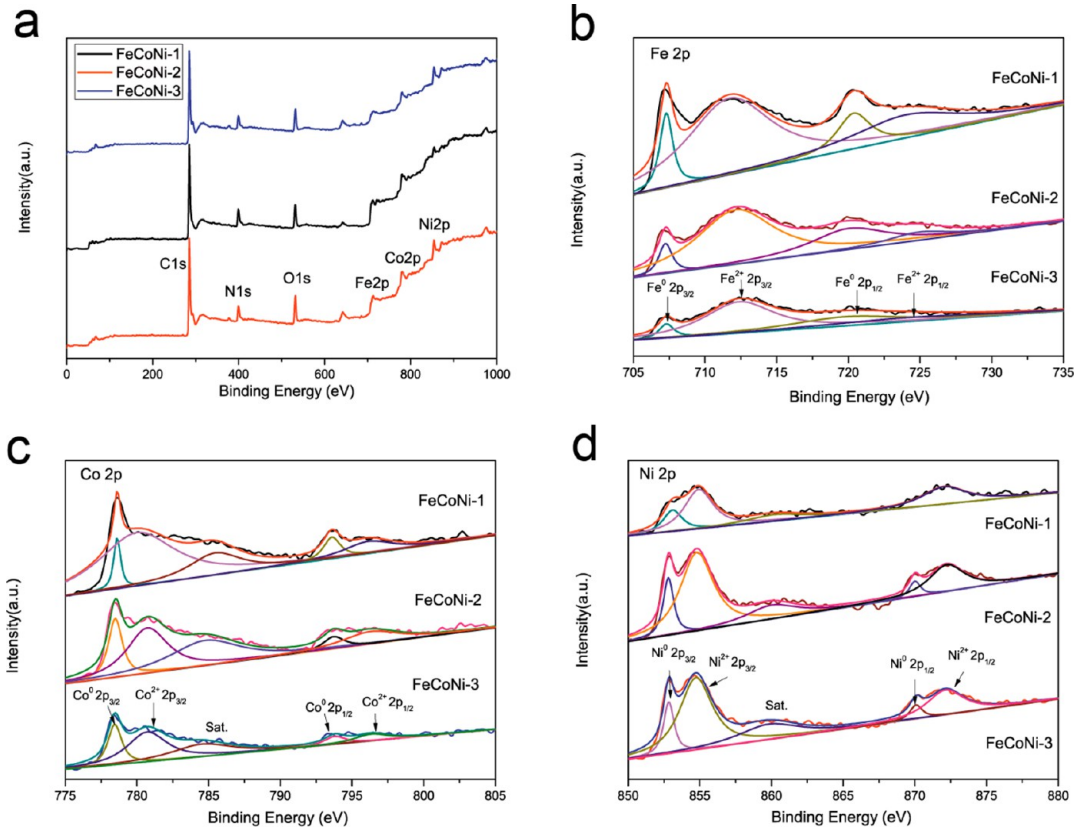

Figure 4. (a) XPS spectra of FeCoNi-1, FeCoNi-2, and FeCoNi-3. Wide spectra and high-resolution spectra of (b) Co 2p, (c) Fe 2p, and (d) Ni 2p.

DOI: 10.1021/acscatal.6b02573
ACS Catal. 2017, 7, 469–479

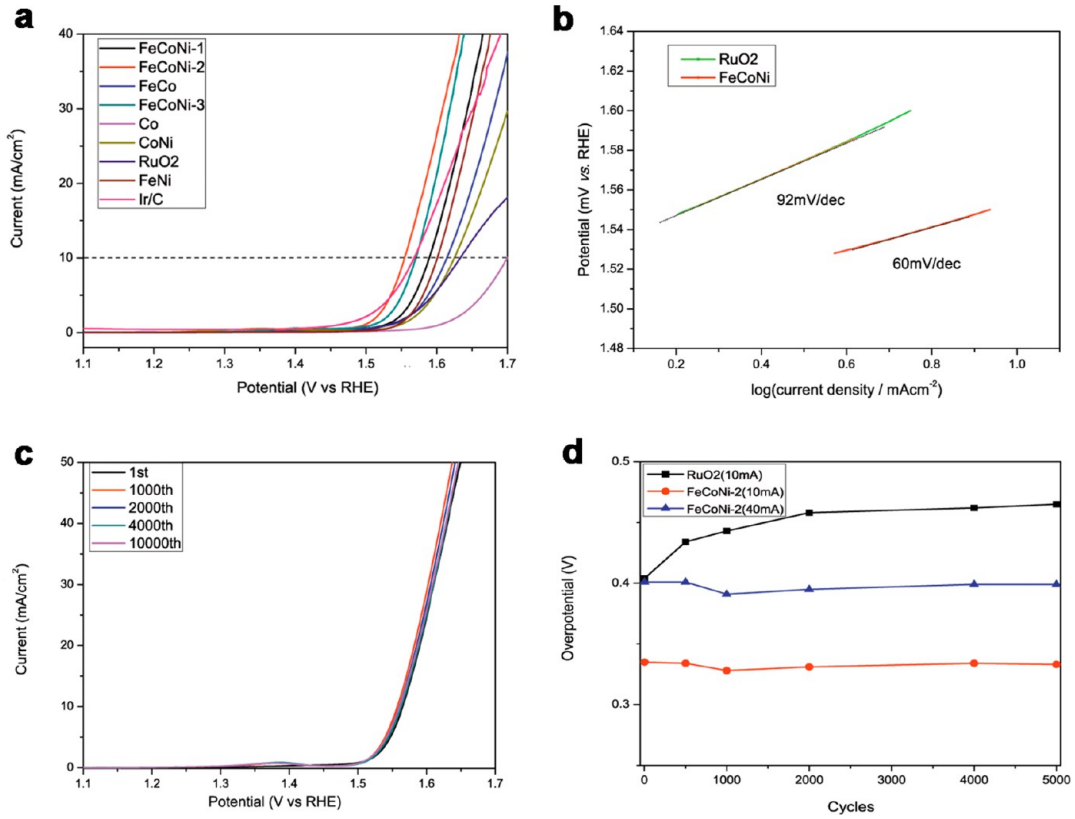

Figure 5. Electrocatalytic OER performance tests of different metals, binary alloys, and ternary alloys in a 1 M KOH solution. (a) OER polarization curves for different metals, binary alloys, and ternary alloys compared with Ir/C and RuO_2 with the same mass loading. (b) Tafel plots for FeCoNi-2 and RuO_2. (c) Durability test of FeCoNi-2 in an alkaline electrolyte for 10000 cycles. (d) Overpotential changes of current densities at 40 and 10 mA cm^{-2} for FeCoNi-2 and in comparison with RuO_2 at 10 mA cm^{-2} during the durability test.

amount of N atoms were doped in the graphene layers (the I_D/I_G ratio of CoNi is relatively lower than those of other alloys, because there are many carbon nanotubes in the sample of CoNi as illustrated in Figure S1e,h). Nitrogen doping has proven to be beneficial for improving the performance of OER and HER.[12] Moreover, the second-order band in all samples is broad and weak, indicating the alloys are encapsulated by thin layers of graphene.[19]

The chemical states of ternary alloys measured by X-ray photoelectron spectroscopy (XPS) are illustrated in Figure 4. Deconvolution of the complex Fe 2p, Co 2p, and Ni 2p spectra (Figure 4b–d, respectively) suggests the presence of two chemically distinct species: the metallic state of Fe (707.3 and 719.8 eV), Co (778.5 and 793.8 eV), and Ni (852.8 and 870.1 eV) and the oxidation state of Fe (712.4 and 724.2 eV), Co (780.7 and 796.3 eV), and Ni (854.7 and 872.1 eV). The results for metallic Fe, Co, and Ni were consistent with our XRD analysis and HRTEM results, while the oxidation state indicates the surfaces of alloys are partially oxidized or interacted with adsorbed O_2. Some MOF-derived metals or alloys encapsulated by graphene also provided similar results.[28−30] In addition, Li and his co-workers have provnd that the majority of metal species maintained the metallic state in Prussian blue analogue-derived core−shell structure through X-ray adsorption near edge structure (XANES) and extended X-ray absorption fine structure (EXAFS) analysis.[28] Interestingly, the metal contents measured by XPS were very low (Table S1). This result is also reasonable, because XPS is sensitive to the surface and thereby is ineffective in detecting signals of the alloy core inside the graphene layers, further proving that alloys were completely encapsulated by graphene layers. The nitrogen contents of three samples were ∼10 atom %, and their N 1s spectrum can be deconvoluted into four individual peaks (Figure S6) that can be assigned to pyridinic N (398.7 eV), pyrrolic N (399.3 and 400.8 eV), and quaternary N (401.3 eV). However, it should be noted that some of the nitrogen might bond with metal atoms in our materials. In particular, pyrrolic N has two binding energies here (399.3 and 400.8 eV), which might be ascribed to the energy shift induced by the interaction of some pyrrolic N with metal atoms.[31,32]

To determine the exact metal proportions in the ternary alloys, we also conducted inductively coupled plasma (ICP) measurement (Table S2). According to the results, we could find that the Co content remains almost unchanged in the three alloys. In addition, the Fe contents will decrease with an increase in Ni content from FeCoNi-1 to FeCoNi-3. This result is also consistent with the metal contents of their corresponding precursor as well as the XRD analysis, proving the successful control of metal proportions via alteration of the amounts of precursors. It should be noted that the exact values of Fe, Co, and Ni in the samples measured by EDX (Table S3 and Figure S7) were different from ICP results. This is reasonable, because ICP results are obtained through dissolution of whole materials; however, EDX results came from some particles near the edge of the sphere. As illustrated in Scheme 1c, even though existing metal atoms interdiffuse during the annealing process, the particles near the edge will still have a Ni content higher than and an Fe content lower than those of the inner part due to the intrinsically different composition between the core and shell. However, the

DOI: 10.1021/acscatal.6b02573
ACS Catal. 2017, 7, 469−479

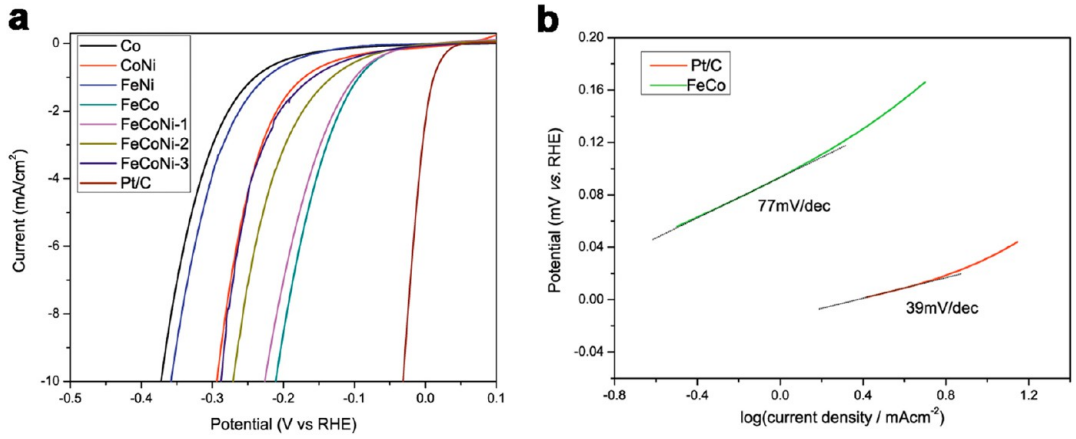

Figure 6. Electrocatalytic HER performance tests of different metals, binary alloys, and ternary alloys in a 1 M KOH solution. (a) HER polarization curves for different metals, binary alloys, and ternary alloys compared with that for Pt/C with the same mass loading. (b) Tafel plots for FeCoNi-2 and Pt/C.

changing tendency of Fe and Ni contents is the same from both ICP and EDX measurements, proving the successful control of metal proportions through tuning the amounts of precursors. The specific surfaces of ternary alloys obtained using the Brunauer–Emmett–Teller (BET) method were listed in Table S4, and our previous study proved there was no direct relationship between electrochemical performance and the difference in specific surface within that range.[12]

The performance of catalysts toward oxygen evolution reaction (OER) was explored in a 1 M KOH solution by a typical three-electrode electrochemical cell. Ag/AgCl (3 M KCl) and platinum foil electrodes were used as the reference electrode and counter electrode, respectively. As illustrated in Figure 5a, we conducted linear sweep voltammograms (LSVs) to assess the activities of the oxygen evolution reaction for metal, binary alloys, and ternary alloys. We also measured the performance of Ir/C (20 wt % Ir on Vulcan carbon black purchased from Premetek Co.) and RuO_2 (Alfa aesar) as references. In general, all catalysts except Co had OER activity much higher than that of RuO_2. Ir/C is superior to most of our alloy samples; however, the overpotential to reach 10 mA/cm^2 of FeCoNi-2 is still lower than that of Ir/C, indicating the excellent OER performance of FeCoNi-2. The overpotential of ternary alloys to reach a current density of 10 mA cm^{-2} is lower than that of the binary alloy and pure metal, indicating that incorporating transition metal and binary alloys into ternary alloys will improve their OER activity. In addition, FeCoNi-2 exhibits the best catalytic performance (overpotential of 325 mV at 10 mA cm^{-2}) among all ternary alloys, proving that further altering metal proportions of ternary alloys could also enhance their properties. The Tafel plot of FeCoNi-2 was recorded and compared with that of RuO_2 (Figure 5b). The Tafel slope of FeCoNi-2 is 60 mV dec^{-1}, which is much lower than that of RuO_2 (92 mV dec^{-1}), showing FeCoNi-2 is a better catalyst for driving the OER process than RuO_2 is at a lower overpotential. The durability of FeCoNi-2 was also assessed by measuring polarization curves after particular cyclic voltammetric (CV) sweeps as illustrated in Figure 5c. The polarization curve of FeCoNi-2 after 10000 cycles retained a performance almost similar to that of the initial test, exhibiting excellent cycling stability. Moreover, from the potential values recorded at different current densities of 10 and 40 mA cm^{-2} before and after the test (Figure 5d), FeCoNi-2 exhibits high stability, obviously superior to the durability of its RuO_2 counterpart. To further prove the material is wholly alloyed, we also obtained a mixture by mechanical mixing of FeCo and CoNi with a precursor ratio that is the same as that of FeCoNi-2. As shown in Figure S8, the mixture of FeCo and CoNi also exhibits OER activity obviously inferior to that of FeCoNi-2, indicating the core of our sample is also successfully alloyed. As illustrated in enlarged Figure 5a (Figure S9), a slight peak emerging around 1.4 V versus RHE might be ascribed to partial oxidation of alloys during cycling according to previous research.[33] However, the peak intensity is relatively lower compared with those of other transition metal-based OER catalysts without the protection of a graphene layer. In addition, the oxidation peak remained almost same after the 1000th cycle, indicating further oxidation was prevented by the graphene layer. We also used the saturated calomel electrode (SCE) as a reference electrode to verify the activity and stability of FeCoNi-2 as an OER catalyst, and the results were compared with those of the Ag/AgCl electrode. The difference between two electrodes of measured overpotentials to a reach current density of 10 mA cm^{-2} is only 5 mV as illustrated in Figure S10a. Besides, a long cycling test using the SCE also shows a similar result with the Ag/AgCl electrode: FeCoNi-2 exhibits negligible activity degradation even after the 10000th cycle, indicating the excellent stability of our catalyst (Figure S10b). The excellent activity as well as stability of FeCoNi-2 makes it a promising alternative for highly active nonprecious metal electrocatalysts for OER.

Utilizing a standard three-electrode electrochemical system, we assess the catalytic activity of samples for HER in 1 M KOH. The electrocatalytic activity of 20 wt % Pt/C (Sigma-Aldrich) was also measured to make a comparison. The polarization curves of the samples are illustrated in Figure 6a. Pt/C is still one of the best HER catalysts in a basic electrolyte; meanwhile, pure Co exhibited relatively poor HER activity. We chose potentials at a current density of 10 mA cm^{-2} as criteria for comparing activities of various catalysts. The potentials increase in the following order: Pt < FeCo < FeCoNi-1 < FeCoNi-2 < FeCoNi-3 < CoNi < FeNi < Co. Unlike the OER test results, the binary FeCo alloy exhibits the best HER catalytic activity among all nonprecious samples, reaching a current density of 10 mA cm^{-2} at low overpotentials of only 211 mV. Tafel plots of the FeCo alloys and Pt/C are shown in

DOI: 10.1021/acscatal.6b02573
ACS Catal. 2017, 7, 469–479

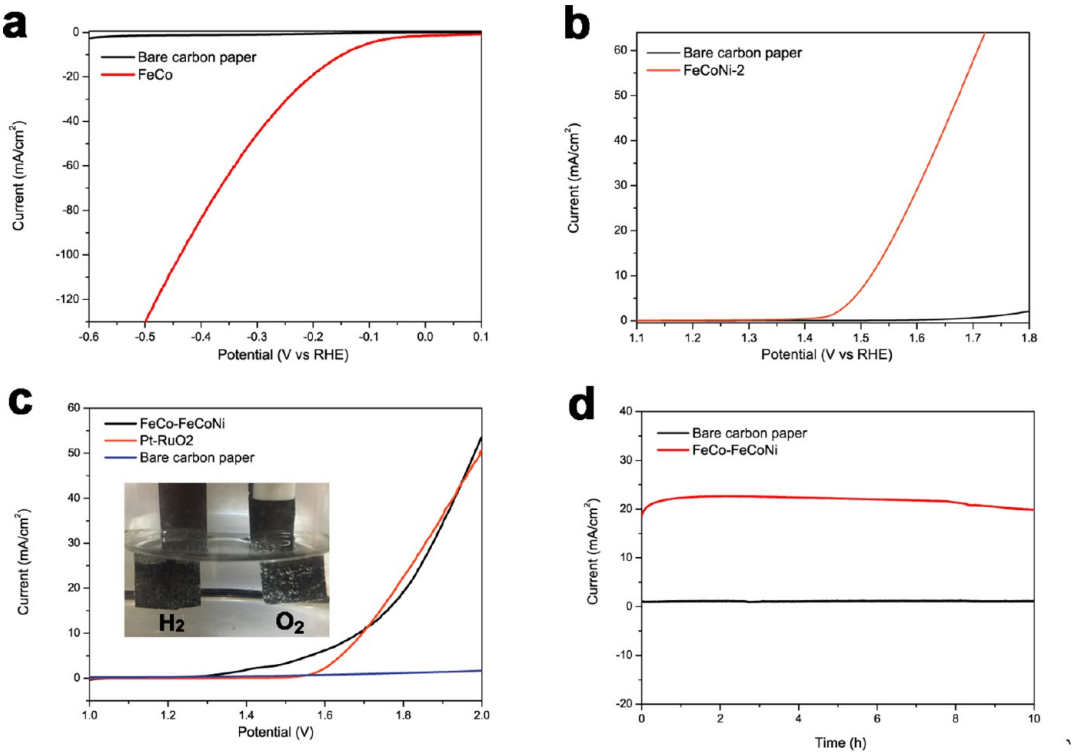

Figure 7. (a) HER polarization curves of FeCo with a loading amount of 1 mg cm^{-2} on carbon paper. (b) OER polarization curves of FeCoNi-2 with a loading amount of 1 mg cm^{-2} on carbon paper. (c) Polarization curves of FeCo/FeCoNi and Pt/RuO_2 catalyst couples for overall water splitting in 1.0 M KOH. The mass loadings of FeCo/FeCoNi-2 and Pt/RuO_2 couples were 1.0 and 0.32 mg cm^{-2}, respectively. The inset is an optical photograph showing the generation of H_2 and O_2 bubbles for FeCo/FeCoNi on carbon paper. (d) Time-dependent current density curves (i–t curve) under static overpotentials of 1.8 V in 1.0 M KOH. During all measurements, the bare carbon papers without catalysts were also measured for comparison.

Figure 6b, which are usually used to reveal the inherent reaction mechanism of HER. The Tafel plot of the FeCo catalyst shows a value of 77 mV dec^{-1}, demonstrating that the HER process is following the Volmer–Heyrovsky mechanism according to previous research.[34] We also measured OER and HER activity of our best catalysts (FeCo and FeCoNi-2) in 0.1 M KOH (Figure S11) and compared them with those measured in 1 M KOH. As shown in Figure S11, both FeCo and FeCoNi-2 exhibit inferior activity in 0.1 M KOH compared to that in 1 M KOH; this phenomenon also exists in other electrocatalysts and even for Pt/C and Ir/C.[35] The TEM images of FeCo and FeCoNi-2 after 10000 HER and OER cycles are also provided. As shown in panels a and c of Figure S12, the electrocatalysts maintained their original morphology after cycling, and from the enlarged TEM images (Figure S12b,d), we can still see the core–shell structure, further confirming the stability of the electrocatalysts.

In the practical application of electrochemical water splitting, the catalysts were usually grown or transferred onto conductive substrates with an increased amount of loading, especially for nonprecious catalysts.[36−38] Therefore, we also measured the catalytic activity of HER and OER of our materials on carbon fiber paper with a loading amount of 1.0 mg/cm^2. Compared with nickel foam or carbon cloth, carbon fiber paper exhibits negligible intrinsic activity, which will weaken the influence of measurement for catalysts.[39−41] As illustrated in panels a and b of Figure 7, bare carbon paper exhibited negligible activity of HER and OER; however, carbon paper loaded with FeCo and FeCoNi-2 catalyst reached a current density of 10 mA cm^{-2} at low potentials of 149 mV for HER and 288 mV for OER, which were extremely excellent among those of nonprecious electrochemical catalysts.[4,6,9,42−54] The comparison of HER and OER activity measured on a glassy carbon electrode and three-dimensional substrates are illustrated in Tables S7 and S8. To demonstrate the practical application of catalysts for overall water splitting, a simple water electrolyzer was measured by using FeCo on carbon paper as a cathode and FeCoNi-2 on carbon paper as an anode. As shown in Figure 7c, a current density of 10 mA cm^{-2} could be achieved by applying a potential of 1.687 V between two electrodes, which is even smaller than that of its Pt-RuO_2 counterpart (1.696 V). The simple water electrolysis exhibited vigorous gas evolution on both electrodes, as shown in the Supplementary Video at a potential of 1.7 V. In addition, the very stable current density at a high potential of 1.8 V in i–t curves (Figure 7d) further demonstrated the strong stability of the alloys. Bare carbon fiber papers were also measured at 1.8 V for comparison. The negligible activity of carbon paper further proved the activity came from the catalysts. The excellent activity of the alloy catalyst, accompanied by high stability, made it a potential alternative for precious catalysts in practical water splitting.

To obtain further perceptions about the relationship between the composition of the alloys and the performance of OER and HER, DFT calculations were further applied using Vienna Ab Initio Simulation Package (VASP). A graphitic carbon cage C_{240} encapsulating 55 metal atoms was used as the basic model of graphene-encapsulated alloys, which also performed well in previous studies.[11,14,16] In general, OER usually follows a four-electron step process in a basic electrolyte as shown in Figure S13a–c.[55]

DOI: 10.1021/acscatal.6b02573
ACS Catal. 2017, 7, 469–479

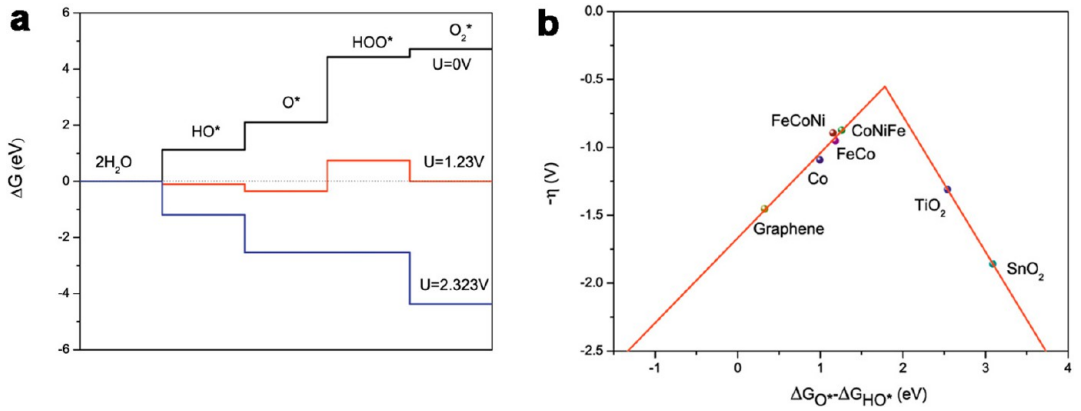

Figure 8. (a) Free energy profiles for the OER over a nitrogen-doped graphene-encapsulated Co cluster at zero potential (U = 0), equilibrium potential for oxygen evolution (U = 1.23 V), and minimal potential (U = 2.32 V) where all steps become downhill. (b) Activity trends toward oxygen evolution reaction, where the negative value of the theoretical overpotential (η) is plotted vs the standard free energy ($\Delta G_{HO*} - \Delta G_{O*}$).

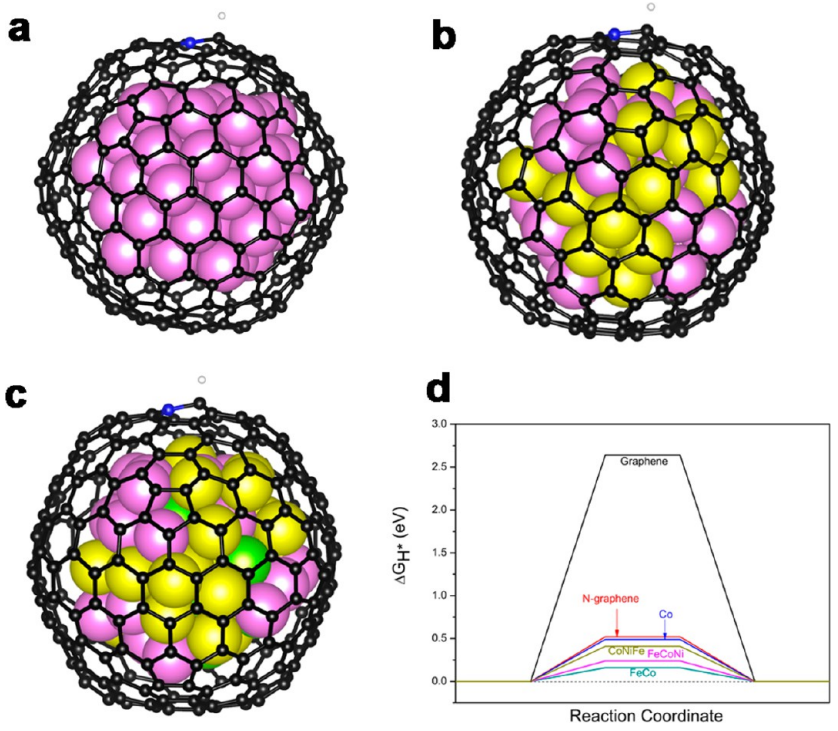

Figure 9. Optimized structures of H* adsorbed on (a) nitrogen-doped graphene-encapsulated Co, (b) the nitrogen-doped graphene-encapsulated FeCo alloy, and (c) the nitrogen-doped graphene-encapsulated FeCoNi alloy. (d) Calculated ΔG_{H*} diagram of different models. The yellow, pink, and green spheres represent Fe, Co, and Ni atoms, respectively.

$$OH^- + * \rightarrow HO* + e^- \quad (1)$$

$$HO* + OH^- \rightarrow H_2O + O* + e^- \quad (2)$$

$$O* + OH^- \rightarrow HOO* + e^- \quad (3)$$

$$HOO* + OH^- \rightarrow O_2* + e^- \quad (4)$$

The energy diagram for the Co oxygen evolution catalyst is shown in Figure 9a, where free energies of various intermediates adsorbed by nitrogen-doped graphene-encapsulated Co at different constant potentials were calculated. The catalytic performance for the OER is determined by potential-determining steps, especially the last step, to become downhill in free energy as the potential increases.[55] As illustrated in Figure 8a, there are some endothermic reaction steps at zero potential and equilibrium potential at 1.23 V. The free energies of all steps become downhill until the potential increases to 2.32 V. This means a 1.09 V overpotential is required for the OER process compared with the equilibrium potential on the catalyst of graphene-encapsulated Co. This result is in good agreement with the experimental result that Co needs a high overpotential for OER. We also calculated free energies of different adsorption steps for other models. We established two models designated as FeCoNi ($Fe_{24}Co_{24}Ni_7$) and CoNiFe ($Fe_{15}Co_{20}Ni_{20}$), which refer to the ternary alloys with lower and higher Ni contents, respectively, to distinguish ternary alloys with different metal proportions. To reduce the cost of calculation, we calculated only models of pure graphene, Co, FeCo, FeCoNi, and CoNiFe, and these results are sufficient to illustrate the trend from metal to ternary alloys; the calculated results are listed in Table S6. The free energy profiles for

DOI: 10.1021/acscatal.6b02573
ACS Catal. 2017, 7, 469−479

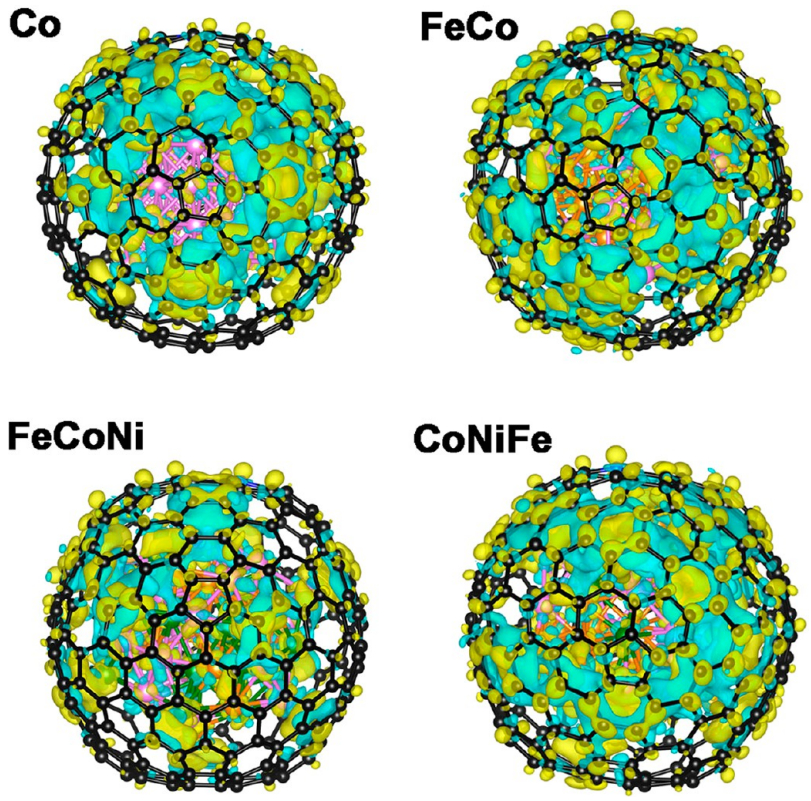

Figure 10. Calculated charge density differences of various models. The isosurface value of the color region is 0.01 e Å^{-3}. The yellow and cyan regions refer to increased and decreased charge distributions, respectively. FeCoNi ($Fe_{24}Co_{24}Ni_7$) and CoNiFe ($Fe_{15}Co_{20}Ni_{20}$) refer to ternary alloys with lower and higher Ni contents, respectively.

models of FeCo, FeCoNi, and CoNiFe alloys are also provided (as illustrated in Figure S14). Searching for the relationship between free energies of species and the overpotentials for different materials is important to the rational design of electrochemical catalysts. Previous studies showed that binding energies of HOO* and HO* intermediates on various surfaces have a universal scaling relation.[11,55] Our calculated results are consistent with them; as illustrated in Table S6, the values of $\Delta G_{HOO*} - \Delta G_{HO*}$ for different models approximate 3.2 eV. Therefore, overpotential η of OER can be plotted as a function of $\Delta G_{O*} - \Delta G_{HO*}$ for different models examined here, which will provide a general volcano relationship between different catalyst materials as illustrated in Figure 8b (the values of metal oxides were taken from ref 55). According to the volcano plot, we could find the OER activity is increasing to approach the summit through incorporation of transition metals into binary and ternary alloys (increasing the degrees of freedom for alloys), which is in good agreement with our experimental results. Furthermore, changing the metal proportion of Fe, Co, and Ni in ternary alloys will also influence the overpotential of catalysts.

We also investigated the HER activity of different alloys through DFT calculations. Compared with that of the HER in acids, the reactant in bases is water instead of hydronium. However, adsorbed hydrogen (H_{ad}) is still the reaction intermediate on the catalyst surface, which is similar to the situation in an acidic electrolyte.[56] Therefore, ΔG_{H*} is usually employed as a key descriptor in predicting theoretical activity for hydrogen evolution reaction in an alkaline electrolyte. A moderate free energy of ~0 eV would lead to optimal HER activity with a lower reaction barrier because of the balance between the adsorption and desorption steps.[57] We calculated the ΔG_{H*} values of various models, including pure graphene, nitrogen-doped graphene, graphene-encapsulated metal (Co), binary alloys (CoFe), and ternary alloys (FeCoNi and CoNiFe). The optimized structures of H adsorption at Co, CoFe, and FeCoNi encapsulated by nitrogen-doped graphene are illustrated in panels a–c of Figure 9, respectively. The calculated HER free energy diagrams are shown in Figure 9d, which are in good agreement with experimental results: graphene-encapsulated binary and ternary alloys exhibit HER performance better than that of pure metal. The FeCo alloy possesses the smallest ΔG_{H*} that is closest to zero, followed by those of FeCoNi and CoNiFe ternary alloys, indicating that a decrease in Ni content in ternary alloys will improve the performance of HER in an alkaline solution. The diagrams also show that nitrogen doping can significantly lower the binding energy of pure graphene, which is consistent with previous studies. Because the nitrogen contents among alloys are similar (Table S1), difference ΔG_{H*} would mainly derive from the unique electronic structures of various alloys.

The electronic structure of the material surface is a key parameter for electrochemical activity. To further reveal the origin of the difference in activity between various catalysts in HER and OER, Bader charge analysis as well as charge density difference analysis was employed.[58] As shown in Figure 10, there is charge transfer from metal to the graphene layer in various models. Previous studies proved that the surface electron distribution of a metal or alloy could be modified by the strain or ligand effects originating from the introduction of another metal heteroatom.[59−61] Because catalytic reactions mainly occus at the graphene surface in our catalysts, the

DOI: 10.1021/acscatal.6b02573
ACS Catal. 2017, 7, 469−479

change in electronic structure for graphene altered by the different number of electrons being transferred from the metal core (as listed in Table S5) will lead to different binding energies of reaction intermediates. As for HER, pure graphene exhibited weak ability to bind H* as shown in Figure 9d, and the electrons transferred from metal to C atoms were beneficial for enhancing C−H binding, improving HER activity as a whole. Therefore, the FeCo model with the most transferred electrons (6.69e$^-$) exhibits the best HER performance. With respect to OER, the overpotential is determined by the relative value between ΔG_{O*} and ΔG_{HO*}, and a proper number of transferred electrons might result in the optimal value of $\Delta G_{O*} - \Delta G_{HO*}$ in the volcano plot, thereby enhancing OER activity.

In summary, we developed a facile and universal method for preparing nitrogen-doped graphene with uniform 3d transition metal, binary alloys, and ternary alloys being encapsulated by direct annealing of different MOFs. When the amount of precursors is controlled, the metal proportions in ternary alloys can also be tuned intentionally. The electrochemical measurements show that incorporating a third transition metal into a binary alloy (increasing the degrees of freedom of alloys) can lead to the enhancement of OER activity. In addition, for HER catalysts in an alkaline solution, with a decrease in the Ni content of ternary FeCoNi alloys, HER performance can also be improved. DFT calculations indicate that the change in alloy composition and proportion will change the number of transferred electrons between alloys and graphene, thereby tuning electronic structures of graphene-encapsulated alloys and influencing HER and OER activity. These findings provide new insight into the rational design of efficient nonprecious OER and HER catalysts via an increase or decrease in the degrees of freedom of alloys. Besides, the universal and facile method will provide new insight into the synthesis of other electrochemical catalysts.

■ ASSOCIATED CONTENT

Supporting Information

The Supporting Information is available free of charge on the ACS Publications website at DOI: 10.1021/acscatal.6b02573.

Detailed experimental process, SEM, TEM, and HRTEM images, elemental mapping, EDX, XPS spectra, supplementary electrochemical measurements and details, and calculation details (PDF)

Supplementary video (AVI)

■ AUTHOR INFORMATION

Corresponding Author

*E-mail: cqw@ustc.edu.cn.

ORCID

Yang Yang: 0000-0002-1516-0627

Jitang Chen: 0000-0002-1607-7075

Funding

This study was supported by the National Natural Science Foundation (NSFC, 21271163 and U1232211), the Fundamental Research Funds for the Central Universities (WK2060140021) and the CAS/SAFEA International Partnership Program for Creative Research Teams and the Hefei Science Center CAS (2016HSC-IU011).

Notes

The authors declare no competing financial interest.

■ ACKNOWLEDGMENTS

The calculations were completed on the supercomputing system in the Supercomputing Center of the University of Science and Technology of China.

■ REFERENCES

(1) Lai, J. P.; Li, S. P.; Wu, F. X.; Saqib, M.; Luque, R.; Xu, G. B. *Energy Environ. Sci.* **2016**, *9*, 1210−1214.

(2) Hou, Y.; Lohe, M. R.; Zhang, J.; Liu, S. H.; Zhuang, X. D.; Feng, X. L. *Energy Environ. Sci.* **2016**, *9*, 478−483.

(3) Jin, H. Y.; Wang, J.; Su, D. F.; Wei, Z. Z.; Pang, Z. F.; Wang, Y. *J. Am. Chem. Soc.* **2015**, *137*, 2688−2694.

(4) Zhu, H.; Zhang, J. F.; Yanzhang, R. P.; Du, M. L.; Wang, Q. F.; Gao, G. H.; Wu, J. D.; Wu, G. M.; Zhang, M.; Liu, B.; Yao, J. M.; Zhang, X. W. *Adv. Mater.* **2015**, *27*, 4752−4759.

(5) Gong, M.; Zhou, W.; Tsai, M. C.; Zhou, J. G.; Guan, M. Y.; Lin, M. C.; Zhang, B.; Hu, Y. F.; Wang, D. Y.; Yang, J.; Pennycook, S. J.; Hwang, B. J.; Dai, H. J. *Nat. Commun.* **2014**, *5*, 4695.

(6) Zou, X. X.; Huang, X. X.; Goswami, A.; Silva, R.; Sathe, B. R.; Mikmekova, E.; Asefa, T. *Angew. Chem., Int. Ed.* **2014**, *53*, 4372−4376.

(7) Gong, M.; Dai, H. J. *Nano Res.* **2015**, *8*, 23−39.

(8) Tavakkoli, M.; Kallio, T.; Reynaud, O.; Nasibulin, A. G.; Johans, C.; Sainio, J.; Jiang, H.; Kauppinen, E. I.; Laasonen, K. *Angew. Chem., Int. Ed.* **2015**, *54*, 4535−4538.

(9) Wang, J.; Gao, D. F.; Wang, G. X.; Miao, S.; Wu, H. H.; Li, J. Y.; Bao, X. H. *J. Mater. Chem. A* **2014**, *2*, 20067−20074.

(10) Galan-Mascaros, J. R. *ChemElectroChem* **2015**, *2*, 37−50.

(11) Cui, X. J.; Ren, P. J.; Deng, D. H.; Deng, J.; Bao, X. H. *Energy Environ. Sci.* **2016**, *9*, 123−129.

(12) Yang, Y.; Lun, Z. Y.; Xia, G. L.; Zheng, F. C.; He, M. N.; Chen, Q. W. *Energy Environ. Sci.* **2015**, *8*, 3563−3571.

(13) Chen, P. Z.; Xu, K.; Fang, Z. W.; Tong, Y.; Wu, J. C.; Lu, X. L.; Peng, X.; Ding, H.; Wu, C. Z.; Xie, Y. *Angew. Chem., Int. Ed.* **2015**, *54*, 14710−14714.

(14) Deng, J.; Ren, P.; Deng, D.; Yu, L.; Yang, F.; Bao, X. *Energy Environ. Sci.* **2014**, *7*, 1919−1923.

(15) Wang, J. H.; Cui, W.; Liu, Q.; Xing, Z. C.; Asiri, A. M.; Sun, X. P. *Adv. Mater.* **2016**, *28*, 215−230.

(16) Deng, J.; Ren, P. J.; Deng, D. H.; Bao, X. H. *Angew. Chem., Int. Ed.* **2015**, *54*, 2100−2104.

(17) Du, N. N.; Wang, C. M.; Wang, X. J.; Lin, Y.; Jiang, J.; Xiong, Y. J. *Adv. Mater.* **2016**, *28*, 2077−2084.

(18) Yu, X. Y.; Feng, Y.; Guan, B. Y.; Lou, X. W.; Paik, U. *Energy Environ. Sci.* **2016**, *9*, 1246−1250.

(19) Zheng, F. C.; Yang, Y.; Chen, Q. W. *Nat. Commun.* **2014**, *5*, 5261.

(20) Liu, B.; Shioyama, H.; Akita, T.; Xu, Q. *J. Am. Chem. Soc.* **2008**, *130*, 5390−5391.

(21) Zhang, L.; Wu, H. B.; Lou, X. W. *J. Am. Chem. Soc.* **2013**, *135*, 10664−10672.

(22) Xia, B. Y.; Yan, Y.; Li, N.; Wu, H. B.; Lou, X. W. D.; Wang, X. *Nature Energy* **2016**, *1*, 15006.

(23) Huang, G.; Zhang, L. L.; Zhang, F. F.; Wang, L. M. *Nanoscale* **2014**, *6*, 5509−5515.

(24) Guan, B. Y.; Yu, L.; Lou, X. W. *Energy Environ. Sci.* **2016**, *9*, 3092−3096.

(25) Chen, L. Y.; Bai, J. F.; Wang, C. Z.; Pan, Y.; Scheer, M.; You, X. Z. *Chem. Commun.* **2008**, 1581−1583.

(26) Yoo, B. Y.; Hernandez, S. C.; Park, D. Y.; Myung, N. V. *Electrochim. Acta* **2006**, *51*, 6346−6352.

(27) Wu, H. Q.; Xu, D. M.; Wang, Q.; Wang, Q. Y.; Su, G. Q.; Wei, X. W. *J. Alloys Compd.* **2008**, *463*, 78−83.

(28) Zeng, M.; Liu, Y. L.; Zhao, F. P.; Nie, K. Q.; Han, N.; Wang, X. X.; Huang, W. J.; Song, X. N.; Zhong, J.; Li, Y. G. *Adv. Funct. Mater.* **2016**, *26*, 4397−4404.

(29) Hou, Y.; Wen, Z. H.; Cui, S. M.; Ci, S. Q.; Mao, S.; Chen, J. H. *Adv. Funct. Mater.* **2015**, *25*, 872−882.

DOI: 10.1021/acscatal.6b02573
ACS Catal. 2017, 7, 469−479

(30) Wang, T.; Zhou, Q. Y.; Wang, X. J.; Zheng, J.; Li, X. G. *J. Mater. Chem. A* **2015**, *3*, 16435−16439.
(31) Artyushkova, K.; Kiefer, B.; Halevi, B.; Knop-Gericke, A.; Schlogl, R.; Atanassov, P. *Chem. Commun.* **2013**, *49*, 2539−2541.
(32) Zhong, H. X.; Wang, J.; Zhang, Y. W.; Xu, W. L.; Xing, W.; Xu, D.; Zhang, Y. F.; Zhang, X. B. *Angew. Chem., Int. Ed.* **2014**, *53*, 14235−14239.
(33) Smith, R. D. L.; Prevot, M. S.; Fagan, R. D.; Trudel, S.; Berlinguette, C. P. *J. Am. Chem. Soc.* **2013**, *135*, 11580−11586.
(34) Zheng, Y.; Jiao, Y.; Jaroniec, M.; Qiao, S. Z. *Angew. Chem., Int. Ed.* **2015**, *54*, 52−65.
(35) Liu, Y. Y.; Wang, H. T.; Lin, D. C.; Liu, C.; Hsu, P. C.; Liu, W.; Chen, W.; Cui, Y. *Energy Environ. Sci.* **2015**, *8*, 1719−1724.
(36) Li, Y.; Zhao, C. *Chem. Mater.* **2016**, *28*, 5659−5666.
(37) Liang, H.; Shi, H.; Zhang, D.; Ming, F.; Wang, R.; Zhuo, J.; Wang, Z. *Chem. Mater.* **2016**, *28*, 5587−5591.
(38) Wang, H. T.; Lee, H. W.; Deng, Y.; Lu, Z. Y.; Hsu, P. C.; Liu, Y. Y.; Lin, D. C.; Cui, Y. *Nat. Commun.* **2015**, *6*, 7261.
(39) Jin, Y.; Wang, H.; Li, J.; Yue, X.; Han, Y.; Shen, P. K.; Cui, Y. *Adv. Mater.* **2016**, *28*, 3785−3790.
(40) Kong, D. S.; Wang, H. T.; Lu, Z. Y.; Cui, Y. *J. Am. Chem. Soc.* **2014**, *136*, 4897−4900.
(41) Chen, P.; Xu, K.; Tao, S.; Zhou, T.; Tong, Y.; Ding, H.; Zhang, L.; Chu, W.; Wu, C.; Xie, Y. *Adv. Mater.* **2016**, *28*, 7527−7532.
(42) Feng, L. L.; Yu, G. T.; Wu, Y. Y.; Li, G. D.; Li, H.; Sun, Y. H.; Asefa, T.; Chen, W.; Zou, X. X. *J. Am. Chem. Soc.* **2015**, *137*, 14023−14026.
(43) Tang, C.; Wang, H. S.; Wang, H. F.; Zhang, Q.; Tian, G. L.; Nie, J. Q.; Wei, F. *Adv. Mater.* **2015**, *27*, 4516−4522.
(44) Wang, J.; Wu, H. H.; Gao, D. F.; Miao, S.; Wang, G. X.; Bao, X. H. *Nano Energy* **2015**, *13*, 387−396.
(45) Du, S. C.; Ren, Z. Y.; Zhang, J.; Wu, J.; Xi, W.; Zhu, J. Q.; Fu, H. G. *Chem. Commun.* **2015**, *51*, 8066−8069.
(46) Han, L.; Yu, X. Y.; Lou, X. W. *Adv. Mater.* **2016**, *28*, 4601−4605.
(47) Dou, S.; Tao, L.; Huo, J.; Wang, S. Y.; Dai, L. M. *Energy Environ. Sci.* **2016**, *9*, 1320−1326.
(48) Ledendecker, M.; Clavel, G.; Antonietti, M.; Shalom, M. *Adv. Funct. Mater.* **2015**, *25*, 393−399.
(49) Jin, Y.; Wang, H.; Li, J.; Yue, X.; Han, Y.; Shen, P. K.; Cui, Y. *Adv. Mater.* **2016**, *28*, 3785−3790.
(50) You, B.; Jiang, N.; Sheng, M. L.; Gul, S.; Yano, J.; Sun, Y. J. *Chem. Mater.* **2015**, *27*, 7636−7642.
(51) Vrubel, H.; Hu, X. L. *Angew. Chem., Int. Ed.* **2012**, *51*, 12703−12706.
(52) Zhang, S.; Yu, X. B.; Yan, F.; Li, C. Y.; Zhang, X. T.; Chen, Y. J. *J. Mater. Chem. A* **2016**, *4*, 12046−12053.
(53) Fei, H. L.; Yang, Y.; Peng, Z. W.; Ruan, G. D.; Zhong, Q. F.; Li, L.; Samuel, E. L. G.; Tour, J. M. *ACS Appl. Mater. Interfaces* **2015**, *7*, 8083−8087.
(54) Wang, Y.; Nie, Y.; Ding, W.; Chen, S. G.; Xiong, K.; Qi, X. Q.; Zhang, Y.; Wang, J.; Wei, Z. D. *Chem. Commun.* **2015**, *51*, 8942−8945.
(55) Man, I. C.; Su, H. Y.; Calle-Vallejo, F.; Hansen, H. A.; Martinez, J. I.; Inoglu, N. G.; Kitchin, J.; Jaramillo, T. F.; Norskov, J. K.; Rossmeisl, J. *ChemCatChem* **2011**, *3*, 1159−1165.
(56) Durst, J.; Siebel, A.; Simon, C.; Hasche, F.; Herranz, J.; Gasteiger, H. A. *Energy Environ. Sci.* **2014**, *7*, 2255−2260.
(57) Sheng, W. C.; Myint, M.; Chen, J. G. G.; Yan, Y. S. *Energy Environ. Sci.* **2013**, *6*, 1509−1512.
(58) Bader, R. F. W.; Carroll, M. T.; Cheeseman, J. R.; Chang, C. *J. Am. Chem. Soc.* **1987**, *109*, 7968−7979.
(59) Rodriguez, J. *Surf. Sci. Rep.* **1996**, *24*, 223−287.
(60) Chen, J. G.; Menning, C. A.; Zellner, M. B. *Surf. Sci. Rep.* **2008**, *63*, 201−254.
(61) Staszak-Jirkovský, J.; Malliakas, C. D.; Lopes, P. P.; Danilovic, N.; Kota, S. S.; Chang, K.-C.; Genorio, B.; Strmcnik, D.; Stamenkovic, V. R.; Kanatzidis, M. G.; Markovic, N. M. *Nat. Mater.* **2015**, *15*, 197−203.

DOI: 10.1021/acscatal.6b02573
ACS Catal. 2017, 7, 469−479